International Journal of Enhanced Research in Science, Technology & Engineering
ISSN: 2319-7463, Vol. 8 Issue 1, January -2019, Impact Factor: 4.059

Synthesis of Titanium dioxide nanoparticle using Aero-gel method

Dypsy

Department of Chemistry, GCG Sec-14, Gurugram, 122001

* Corresponding, Email ID – dipsikhapra@gmail.com

ABSTRACT

This paper describes a one-pot synthesis of anatase phase titanium dioxide nanoparticles with surface area. The porous titanium dioxide nanoparticles have a quick response (3 s) and fast recovery (1.7 s), with low hysteresis (<1%) and good stability in the 15-98% RH range. The relationship between %RH and resistance was found to be linear, while sensitivity rose with %RH.

Keywords: Nanoparticles, Aero-gel method, metal oxides, humidity sensor

INTRODUCTION

Nanotechnology has emerged as a significant futuristic instrument with the potential to change industries such as electronics, catalysis, sensors, adsorbents, and energy storage. Humidity sensors have attracted a lot of attention since they are used in a variety of industries, including food storage, electronics, agriculture, medicines, and aviation.[1]An ideal humidity sensor should have a fast reaction and recovery time, minimal hysteresis, repeatability, linearity, thermal stability, and the capacity to operate across a greater humidity range. Porous materials can be used to create efficient sensors by allowing water molecules to infiltrate and disperse through their surface, increasing sensitivity.[2]

Fig1. Structure of Nanoparticles

Titanium dioxide has recently emerged as a key n-type semiconductor counterpart material in humidity/gas sensing. Specifically, Titanium dioxide nanoparticles (NPs) have acquired importance as gas and %RH detecting materials.[3-5] Previously, TiO_2 has been produced via sol-gel/hydro-thermal or template/surfactant processes and combined with various metals and metal oxides for use in humidity sensing applications.[6]Furthermore, because of its interesting properties such as thermal stability, chemical resistance, and mechanic template removal, the time duration of synthesis is unnecessarily increased, whereas surfactant removal with multiple washings may lead to agglomeration and reduce the physical properties of nanoparticles suchas bulk density and, most importantly, porosity.[7]

According to earlier reported articles, the particle sizes of TiO_2 NP-based humidity sensors were greater than 5 nm, with less porosity and a clunky structure. This will undoubtedly reduce the efficiency of sensors.With reference to previously published publications, TiO_2 NP-based humidity sensors had particle sizes greater than 5 nm, less porosity, and an awkward shape. This will undoubtedly reduce the sensors' efficiency.[8]In this work, we have synthesized TiO_2 NPs via aero-gel technique to solve these challenges. This process has the benefit of producing large aspect ratio, extremely fine size, and enormous porosity in a very short amount of time.[9] These characteristics are linked to the supercritical drying process, which reduces the capillary action and causes the pores to collapse, forming an ultrafine structure with low density, porosity, and defects like kinks, crystals, corners, and ion vacancies[10-12]With diameters ranging from 5 to 15 nm and a considerable interlayer spacing, the produced TiO_2 NPs had a heterogeneous morphology, with spherical, rectangular, and hexagonal shapes. TiO_2 nanoparticles containing lattice oxygen and a

high number of surface hydroxyl groups were found to be in both the trivalent and tetravalent electronic states by XPS analysis, which has a substantial impact on their ability to sense humidity. TiO_2 NPs exhibit outstanding humidity sensing properties because to their quick response time of 3s, short recovery time of 2s, low hysteresis (<1%), and long-term stability throughout a wide range of 16–96% of applicability.

Experimental

We combined ethanol (99.9% pure) and toluene (HPLC grade) in a 1:1.8 ratio with 40 mM titanium isopropoxide (Sigma Aldrich) and double-distilled water (stoichiometric quantity). A Parr reactor was filled with the mixture after it had been agitated for ten to fifteen minutes. When the aliquot was first heated at 2 °C per minute, N_2gas (200 pressure) was poured. The solvents were gradually withdrawn and allowed to cool to room temperature until the temperature reached 320 °C and the pressure exceeded 1000 psi. At last, a very fine, low density white powder known as Titanium dioxide NPs was produced. It was then sealed up and stored for later use.

RESULTS AND DISCUSSION

A powder X-ray diffraction pattern, which reveals diffraction peaks at (101), (004), (200), (105), (211), (204), (116), (220), and (215) planes, reveals the crystal phase structure of TiO_2 NPs in Fig. 2(a). Per JCPDS file no. #84-1286, all the peaks were assigned to the anatase phase of as Titanium dioxide NPs. The lower crystal size of as Titanium dioxide NPs may be the cause of the broadening of the diffraction peaks. Fig. 2(b) shows an image captured by a high resolution transmission electron microscope (HRTEM) showing mixed morphology (spherical, hexagonal, and rectangular shaped) as Titanium dioxide NPs within the 4–15 nm range. Lattice fringes of as Titanium dioxide NPs are clearly visible in the HRTEM image in Figure 2(c), and the d-spacing for these particles was determined to be 0.318 nm. The crystalline character of as Titanium dioxide NPs was demonstrated by the selected area electron diffraction (SAED) pattern (inset). The morphology of the synthesized as Titanium dioxide NPs, as determined by SEM analysis, is displayed in Fig. S1(a). Numerous spherical clusters of nanoparticles ranging in size from 5 to 15 nm were found, as can be shown.

The N_2 sorption isotherms and pore size distribution (inset) curves for the TiO_2 NPs are shown in Fig. S1(b)†. It is evident that the hysteresis loop is a type IV mesopore structure and an H_3 type loop with slit pore geometry and a limited pore size distribution. It was discovered that the pore diameter ranged from 11–14 nm and the specific surface area was 125 m_2 g−1. When compared to TiO_2 NPs made via traditional hydro-thermal or solvo thermal methods, the aerogel-prepared TiO_2 NPs show a smaller particle size and a higher surface area. The X-ray photoelectron spectroscopy (XPS) measurementwas used to determine the valence state and composition of TiO_2NPs. Fig.3 represents the graph between binding energy and intensity of TiO_2NPs and explains he elements and associated chemical bonds in the top few atomic layer soft he material.

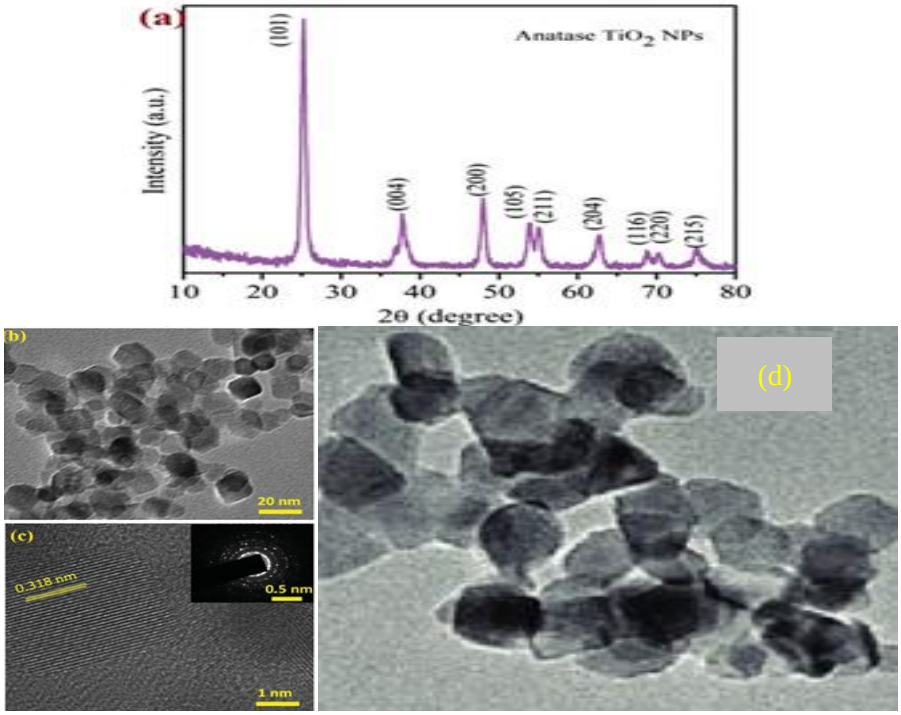

Fig. 2 (a) X-ray diffraction patterns of TiO2 NPs; (b) HRTEM images of TiO2 NPs; (c) interlayer distance and lattice fringes, (inset) selected area diffraction pattern of TiO2 NPs. (d) TEM images of nps

The high resolution XPS spectrum in Figure 3(a) shows two peaks of the doublet of Ti 2p that result from spin–orbit splitting. These peaks could be further deconstructed into four parts: (i) Ti 2p1/2 (474.2 ± 0.2 eV) and (465 ± 0.5 eV) representing Ti3+ {blue color in Fig. 3(a)} and Ti4+ {pink color in Fig. 2(a)}, respectively, and (ii) Ti 2p3/2 (448.6 ± 0.5 eV) and (459.7 ± 0.2 eV) indicating $Ti3^{+}$ and $Ti4^{+}$, respectively.[13-16] The major peak of the O 1s spectrum in Fig. 3(b) is located at 539.9 ± 0.5 eV and is associated with lattice oxygen. A second peak was detected at 521.8 ± 0.2 eV, which has slightly higher binding energy and belongs to the surface hydroxyl group[17]

FT-IR spectroscopy might be used to further support the high surface wettability of TiO_2 NPs; Fig. S2† shows the inorganic vibration bands, such as O–Ti–O, at approximately 430 cm^{-1}. The band peaks at 3383 and 1631 originate from the terminal hydroxyl groups of TiO_2 NPs or adsorbed water molecules, which are strongly determined by the RH environment surrounding the material.[17-18]

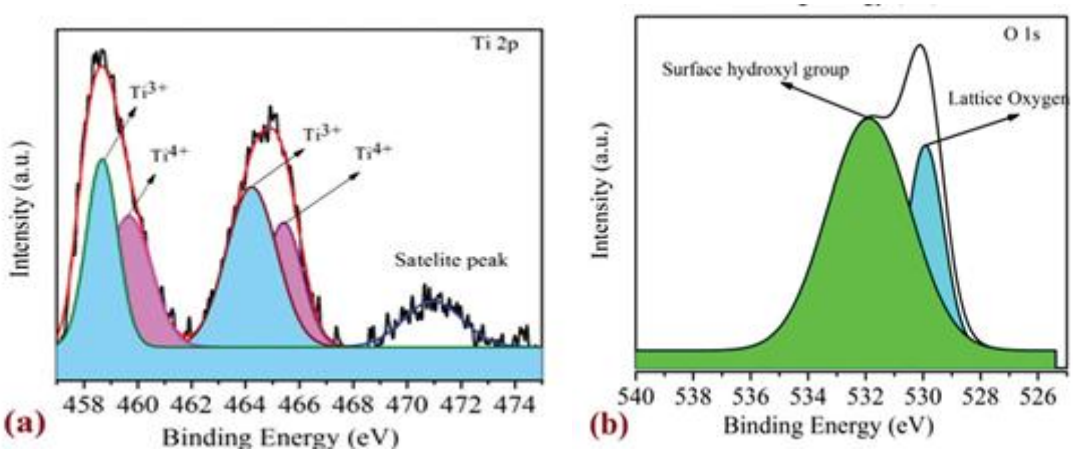

.

Fig 3. Ti 2p core level XPS spectrum of titanium dioxide NPs (b) O 1s spectrum.

Fig. S3† shows the photoluminescence (PL) spectrum of the TiO_2 NPs excited at 250 nm. The small peak appearing at 406 nm is a characteristic peak for the surface recombination of anatase TiO_2 NPs.[19] The two blue emission peaks centered at 437 nm and 498 nm and one green emission peak at 546 nm are assigned to the shallow trapped oxygen vacancy associated with Ti^{3+} centers.[20] Using the resistance variance method, the humidity sensing performance of TiO_2 NPs was tested in the range of 11–98%RH. Significant sensing metrics, including response/recovery time, linearity, sensitivity, hysteresis loss, and stability, have been studied. A toggle switch between the source voltage and sensor electrodes was used to assess the %RH sensing attributes. This switch was manually switched at a frequency of approximately 2Hz to prevent the polarization effect, which in the resistance variance method appears to deteriorate the sensor's performance. Therefore, the polarity reverses as soon as polarization appears, leading to the opposite motion of charge carriers and the nullification of the polarization effect. The response and recovery times are defined as the time taken by the sensor to achieve 90% of the total resistance change during the process of adsorption and desorption, respectively. Fig. 4(a) shows that the response time of TiO_2 NPs(humidification from 11 to 98%RH) was 3s and the recovery time (desiccation from 98 to 11%RH) was 1.7s. The results indicated that the TiO_2 NP sensor is characterized by fastresponse and rapid recovery time. A recovery time of a mere 1.5s is appealing, which enables the sensor for the next measurement within a very little span of time. The outstandingresponse/recovery time for TiO_2 NPs could be attributed to theabundantly present oxygen containing hydroxyl groups and large interlayer distances, which enable water adsorption and desorption throughout the reaction.[20-21]

Additionally, it was seen that the resistance value declined monotonically as the percentage RH level was changed from 11% to 98%. This is because the adsorbed water molecules increase the dielectric parameter, which in turn causes the resistance to decrease due to swelling or the capillary effect. Additionally, the space-charge polarization effect is supported by a large number of adsorbed water molecules on the TiO_2 NPs' interface, which also makes it easier for water molecules to diffuse quickly into the NPs' pores and significantly boosts the creation of proton bonds between –OH groups. Fig. 4(b) shows the remarkable linearity of Titanium dioxide NPs. Fig 4(c) shows the relationship between sensitivity and %RH. As can be seen, the %sensitivity increases with increase in %RH, which could be attributed to the attachment of water molecules with the H-bond through hydroxyl groups to the layer by layer infiltration of continuous water adsorption while increasing the %RH.

Fig. 4(d) shows the dynamic responseand recovery of the TiO_2 NP sensor whereby the sensor was exposed to repeated adsorption/desorption cycles between 11 and 98%RH. As can be seen, during the four loops of measurements (11%RH → 98%RH → 11%RH), the response was found to be remarkably reversible and the resistance values at 11 and 98%RH in each loop were realized accurately. A standard variation (S.D.) of

0.5% was obtained during the four loops of measurement, which also endorses the excellent reproducibility of the %RH response.

A superlative humidity sensor should have very tiny or insignificant hysteresis; thus, it is the most important property of a sensing material, indicating consistency by specifying the greatest difference in %RH values between adsorption and desorption processes.

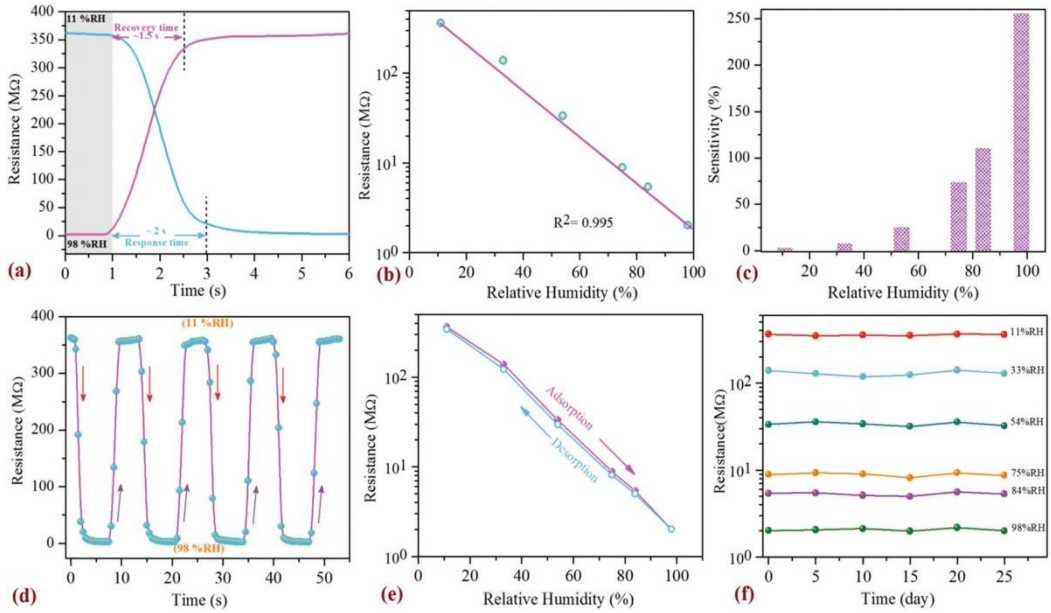

Fig. 4 (a) Response and recovery time of the TiO_2 NPs sensor for humidity levels between 11% RH and 98% RH; (b) linearity of TiO_2 NPs for humidity sensing; (c) sensitivity of TiO_2 NPs for humidity sensing; (d) repeated response and recovery characteristics of TiO_2 NPs; (e) hysteresis curve showing adsorption–desorption responses measured in the 11–98%RH range for TiO_2 NPs; (f) the response of TiO_2 NP sensor monitored under different humidity conditions for 21 days.

The hysteresis error (γH) was determined using the calculation γH + ΔH max, where ΔH 2FFS max represents the difference in adsorption and desorption output and FFS represents the full scale output.[22]Figure 4(e) depicts a typical hysteresis plot of a TiO_2 NP-based sensor, with solid red and green lines representing adsorption (humidification) and desorption (dehumidification), respectively. The adsorption and desorption curves practically overlap, and the sensor has a low hysteresis of <1%, indicating high reliability. The stability of the % RH sensor is a crucial feature for evaluating the potential of humidity sensors in commercial applications. The long-term stability was observed over a period of 27 days by measuring the resistance variation once every 120 hours at 13, 36, 57, 78, 87, and 98% of RH, as shown in Fig. 4f. Excellent long term stability is clearly evident from this figure as the differences in values of resistance were negligible for a particular RH level. The sensor observes an S.D. of 1.9% during the entire span, which reveals the good stability of the sensor. The humidity sensing mechanism of porous materials can be explained by water molecules adsorbed on the surface and capillary water condensation inside the pores of the sensing material. Fig. 5 shows the adsorption phenomenon of water molecules under different %RH conditions. When water molecules get adsorbed onto the surface of a material, conduction is promoted by releasing H^+ and OH^-. Water's high polarity and the presence of two lone pairs of electrons allow it to easily donate H+ and electrons.[25]

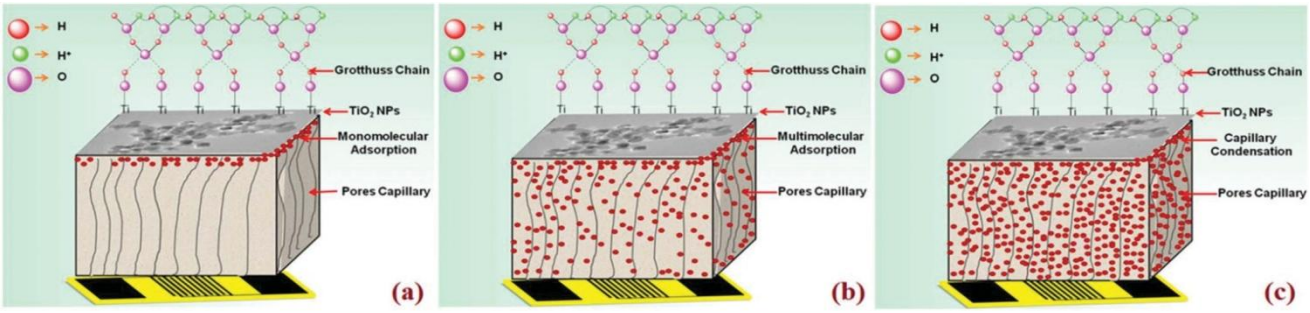

Fig. 5 Mechanism of humidity sensing using TiO_2 NPs, (a) at 11%RH; (b) at intermediate (33%RH) humidity; (c) at maximum (98%RH) humidity

Since water is highly polar and each molecule of water has two lone pairs of electrons, it can easily donate H^+ and electrons.[23] The adsorption of water on the surface of material is divided in two parts: (i) chemisorption and (ii) physisorption. The negatively charged oxygen atom gets attached to positively charged Ti^{3+}/Ti^{4+} ions and leads to the formation of an initial chemisorbed layer of water molecules between positively charged metal ions Ti^{3+}/Ti^{4+} and negatively charged oxygen atoms under the influence of a strong electrostatic field. At low% RH (Fig. 5(a)), water molecules dissociate, forming hydroxyl ions on the sensing material's surface[24], while charge transport is ensured by the chemisorbed hydroxyl group and proton hopping. As the percentage RH increases (Fig. 5(b)), the hydronium ions become a substantial source of charge carriers as the multilayer physisorbed water molecules condense in the capillaries. At the maximum humidity level (98%RH), hydronium ions dissociate into H_2O and H^+ ions (Fig. 5(c)), and each water molecule is impacted by hydrogen bonding and electrostatic interactions between hydroxyl groups.[25-26] Under these conditions, charge carrier transport is followed by the Grotthuss chain reaction, in which the hydronium ion releases H^+ to adjacent water molecules, which accept it and transfer H^+ to their adjacent water molecules, initiating a chain reaction that results in charge transportation across the sensor surface.

CONCLUSIONS

Anatase phase, porous TiO_2 NPs with a high surface area of 117 m_2 g^{-1} and ultrafine size of 5-16 nm were synthesized utilizing a surfactant-free one-pot aerogel technique. The XPS analysis found trivalent and tetravalent oxidation states in TiO_2 NPs with many surface hydroxyl groups. The produced TiO_2 NPs have outstanding %RH sensing capabilities, with fast reaction time (3 s), recovery time (1.7 s), low hysteresis (<1%), and long-term stability in the 15-98%RH range of measurement. TiO_2 NPs have excellent sensing performance due to their porous nature, high surface area, extremely fine size, and long interlayer distance. The innovative findings obtained in this study show that aero-gel.

Conflicts of interest

The authors declare no conflicts of interest.

REFERENCES

[1]. [1] Khan, I.; Saeed, K.; Khan, I. Nanoparticles: Properties, Applications and Toxicities. *Arab. J. Chem.* 2019, *12* (7), 908–931. https://doi.org/10.1016/j.arabjc.2017.05.011.

[2]. [2] Ndolomingo, M. J.; Bingwa, N.; Meijboom, R. Review of Supported Metal Nanoparticles: Synthesis Methodologies, Advantages and Application as Catalysts. *J. Mater. Sci.* 2020, *55* (15), 6195–6241. https://doi.org/10.1007/s10853-020-04415-x.

[3]. [3] Strassburg, S.; Mayer, K.; Scheibel, T. Functionalization of Biopolymer Fibers with Magnetic Nanoparticles. *Phys. Sci. Rev.* 2020, 1–27. https://doi.org/10.1515/psr-2019-0118.

[4]. [4] R.W. Raut, A.S.M. Haroon, Y.S. Malghe, B.T. Nikam, S.B. Kashid, Rapidbiosynthesis of platinum and palladium metal nanoparticles using root extract of asparagus racemosus linn, Adv. Mater. Lett. 4 (2013) 650–654. https://doi.org/10.5185/amlett.2012.11470.

[5]. [5] A.M. El Shafey, Green synthesis of metal and metal oxide nanoparticles from plant leaf extracts and their applications: A review, Green Process. Synth. 9 (2020) 304–339. https://doi.org/10.1515/gps-2020-0031.

[6]. [6] I. E, K. M, D. M, D. S, M. M, Green Biosynthesis of Rhodium Nanoparticles Via Aspalathus Linearis Natural Extract, J. Nanomater. Mol. Nanotechnol. 06 (2017). https://doi.org/10.4172/2324-8777.1000212.

[7]. [7] S. Chouhan, S. Guleria, Green synthesis of AgNPs using Cannabis sativa leaf extract: Characterization, antibacterial, anti-yeast and α-amylase inhibitory activity, Mater. Sci. Energy Technol. 3 (2020) 536–544. https://doi.org/10.1016/j.mset.2020.05.004.

[8]. [8] J. Singh, T. Dutta, K.H. Kim, M. Rawat, P. Samddar, P. Kumar, "Green" synthesis of metals and their oxide nanoparticles: Applications for environmental remediation, J. Nanobiotechnology. 16 (2018) 1–24. https://doi.org/10.1186/s12951-018-0408-4.

[9]. [9] Chaker, H., Fourmentin, S., & Chérif-Aouali, L. (2020). Efficient Photocatalytic Degradation of Ibuprofen under Visible Light Irradiation Using Silver and Cerium Co-Doped Mesoporous TiO2. *ChemistrySelect*, *5*(38), 11787–11796. https://doi.org/10.1002/slct.202002730

[10]. [10] Fauzi, A. A., Jalil, A. A., Hassan, N. S., Aziz, F. F. A., Azami, M. S., Hussain, I., Saravanan, R., & Vo, D. V. N. (2022). A critical review on relationship of CeO2-based photocatalyst towards mechanistic degradation of organic pollutant. *Chemosphere*, *286*(July 2021). https://doi.org/10.1016/j.chemosphere.2021.131651

[11]. [11] Charbgoo, F., Ahmad, M. Bin, & Darroudi, M. (2017). Cerium oxide nanoparticles: Green synthesis and biological applications. *International Journal of Nanomedicine*, *12*, 1401–1413. https://doi.org/10.2147/IJN.S124855

[12]. [12] Arumugam, A., Karthikeyan, C., Haja Hameed, A. S., Gopinath, K., Gowri, S., & Karthika, V. (2015). Synthesis of cerium oxide nanoparticles using Gloriosa superba L. leaf extract and their structural, optical and antibacterial properties. *Materials Science and Engineering C*, *49*, 408–415. https://doi.org/10.1016/j.msec.2015.01.042

[13]. [13] Kannan, S. K., & Sundrarajan, M. (2014). A green approach for the synthesis of a cerium oxide

nanoparticle: Characterization and antibacterial activity. *International Journal of Nanoscience*, *13*(3), 1–7. https://doi.org/10.1142/S0219581X14500185

[14]. [14] Priya, G. S., Kanneganti, A., Kumar, K. A., Rao, K. V., & Bykkam, S. (2014). Bio Synthesis of Cerium Oxide Nanoparticles using Aloe Barbadensis Miller Gel. *International Journal of Scientific and Research Publication*, *4*(6), 1–4.

[15]. [15] Thema, F. T., Letsholathebe, D., & Mphale, K. (2019). Enhanced antibacterial properties of green synthesized nano ceria via Agathosma betulina natural extract. *Materials Today: Proceedings*, *36*, 435–439. https://doi.org/10.1016/j.matpr.2020.05.010

[16]. [16] Thovhogi, N., Diallo, A., Gurib-Fakim, A., & Maaza, M. (2015). Nanoparticles green synthesis by Hibiscus Sabdariffa flower extract: Main physical properties. *Journal of Alloys and Compounds*, *647*, 392–396. https://doi.org/10.1016/j.jallcom.2015.06.076

[17]. [17] Iqbal, A., Ahamad, T., Qais, F. A., Ahmad, N., Shafi, A., Ahmed, A. S., & Srivastava, S. (2013). Proficient visible-light-driven photocatalytic and anti-biofilm activity of biosynthesized CeO2-graphene oxide nanocomposites. *Materials Chemistry and Physics*, *298*(December 2022), 127397. https://doi.org/10.1016/j.matchemphys.2013.127397

[18]. [18] Ganie, A. S., Bashar, N., Bano, S., Hijazi, S., Sultana, S., Sabir, S., & Khan, M. Z. (2014). Development and application of redox active GO supported CeO2/In2O3 nanocomposite for photocatalytic degradation of toxic dyes and electrochemical detection of sulfamaxole. *Surfaces and Interfaces*, *38*(April), 102774. https://doi.org/10.1016/j.surfin.2014.102774

[19]. [19] Mardani, C., Rizal, M. Y., Saleh, R., Taufik, A., & Yin, S. (2015). Synthesis and characterization of Ag/CeO2/graphene nanocomposites as catalysts for water-pollution treatment. *Applied Surface Science*, *530*(March), 147297. https://doi.org/10.1016/j.apsusc.2015.147297

[20]. [20] Alburaih, H. A., Aadil, M., Hassan, W., Amaral, L. S., Ejaz, S. R., Aman, S., & Alsafari, I. A. (2018). Multifunctional Fe and Gd co-doped CeO2-RGO nanohybrid with excellent solar light mediated crystal violet degradation and bactericidal activity. *Synthetic Metals*, *287*(March), 117093. https://doi.org/10.1016/j.synthmet.2018.117093

[21]. [21] Ye, B., Zhao, Z., & Liu, H. (2020). Photocatalytic degradation of Estrone and Congo red by the magnetic antibacterial photocatalyst g-C3N4/CeO2/M-rGO under visible light and optimization by Box-Behnken statistical design (BBD). *Journal of Molecular Structure*, *1272*, 134205. https://doi.org/10.1016/j.molstruc.2020.134205

[22]. [22] Khan, M. E., Khan, M. M., & Cho, M. H. (2017). Ce3+-ion, Surface Oxygen Vacancy, and Visible Light-induced Photocatalytic Dye Degradation and Photocapacitive Performance of CeO2-Graphene Nanostructures. *Scientific Reports*, *7*(1), 1–17. https://doi.org/10.1038/s41598-017-06139-6

[23]. [23] Shanavas, S., Priyadharsan, A., Vasanthakumar, V., Arunkumar, A., Anbarasan, P. M., & Bharathkumar, S. (2017). Mechanistic investigation of visible light driven novel La2CuO4/CeO2/rGO ternary hybrid nanocomposites for enhanced photocatalytic performance and antibacterial activity. *Journal of Photochemistry and Photobiology A: Chemistry*, *340*, 96–108. https://doi.org/10.1016/j.jphotochem.2017.03.002

[24]. [24] Ponnaiah, S. K., Periakaruppan, P., Vellaichamy, B., & Nagulan, B. (2018). Efficacious separation of electron–hole pairs in CeO2-Al2O3 nanoparticles embedded GO heterojunction for robust visible-light driven dye degradation. *Journal of Colloid and Interface Science*, *512*, 219–230. https://doi.org/10.1016/j.jcis.2017.10.058

[25]. [25] Xu, T., Lei, X., Gu, G., Zou, R., & Wu, Q. (2019). Facile synthesis of CeO2-graphene oxide composites with enhanced visible-light photocatalytic performance. *Materials Science and Engineering: B*, *244*(April), 49–55. https://doi.org/10.1016/j.mseb.2019.04.023

[26]. [26] Priyadharsan, A., Vasanthakumar, V., Karthikeyan, S., Raj, V., Shanavas, S., & Anbarasan, P. M. (2017). Multi-functional properties of ternary CeO2/SnO2/rGO nanocomposites: Visible light driven photocatalyst and heavy metal removal. *Journal of Photochemistry and Photobiology A: Chemistry*, *346*, 32–45. https://doi.org/10.1016/j.jphotochem.2017.05.030.